




Structural Optimization of MicroMED Dust Analyzer

Marco Giovanni Corti ¹, Bortolino Saggin ¹, Francesca Esposito ², Gabriele Franzese ², Carmen Porto ², Giuseppe Mongelluzzo ², Fabio Cozzolino ² and Diego Scaccabarozzi ^{1,*}

¹ Department of Mechanical Engineering, Politecnico di Milano—Polo Territoriale di Lecco, 23900 Lecco, Italy; marcogiovanni.corti@polimi.it (M.G.C.); bortolino.saggin@polimi.it (B.S.)

² OAC—Astronomical Observatory of Capodimonte, 80131 Naples, Italy; francesca.esposito@inaf.it (F.E.); gabriele.franzese@inaf.it (G.F.); carmen.porto@inaf.it (C.P.); giuseppe.mongelluzzo@inaf.it (G.M.); fabio.cozzolino@inaf.it (F.C.)

* Correspondence: diego.scaccabarozzi@polimi.it

Featured Application: Aerospace Science and Engineering—Space Science and Engineering.

Abstract: This research work describes the structural optimization of the MicroMED Dust Analyzer, an Optical Particle Counter developed for the ESA ExoMars 2022 mission. Topology Optimization, a non-conventional design technique was adopted to obtain a lighter component, a valuable achievement for aerospace and space scientific instruments design. In particular, two solutions for the instrument optical bench were proposed and assessed relying on a classical finite element approach, comparing the improved performance with the current design. The optimization outcome proved the adopted design workflow robustness and provided promising results in view of a possible mechanical design enhancement of the MicroMED Dust Analyzer instrument. Indeed, a mass budget saving of about 55% of the considered design domain was achieved, and the dynamic behaviour of the optical bench was improved by up to 50% of the first natural frequency value. Finally, a mockup of the lightened optical bench was manufactured, and the redesign effectiveness was proven by comparing the numerical mechanical resonances with the ones obtained experimentally. An error smaller than 5% was found on the first natural frequency, validating the performed optimization approach.

Keywords: MicroMED Dust Analyzer; ExoMars 2022; optical particle counters; topology optimization; thermomechanical design



Citation: Corti, M.G.; Saggin, B.; Esposito, F.; Franzese, G.; Porto, C.; Mongelluzzo, G.; Cozzolino, F.; Scaccabarozzi, D. Structural Optimization of MicroMED Dust Analyzer. *Appl. Sci.* **2023**, *13*, 12810. <https://doi.org/10.3390/app132312810>

Academic Editor: Manoj Gupta

Received: 7 October 2023

Revised: 24 October 2023

Accepted: 27 November 2023

Published: 29 November 2023



Copyright: © 2023 by the authors. Licensee MDPI, Basel, Switzerland. This article is an open access article distributed under the terms and conditions of the Creative Commons Attribution (CC BY) license (<https://creativecommons.org/licenses/by/4.0/>).

1. Introduction

Aerospace components demand lightness as an essential design characteristic, a particularly relevant requirement in the space industry as well. Indeed, mass reduction is considered one of the most valuable drivers during the thermomechanical design of space hardware and aerospace components [1–4]. This objective can be effectively tackled by coupling the choice of high strength-to-density ratio materials with structural optimization, resulting in performant and lightweight components. However, due to their excessively high costs in procurement and manufacturing, qualification, and certification, [5] innovative materials have had low mileage concerning the design of spacecrafts components. Conversely, structural optimization tools played a significant role in the aerospace industry. Optimal design proposals can be obtained by exploiting a streamlined design-to-manufacturing track.

Among the non-conventional thermomechanical design approaches, the Topology Optimization (TO) perfectly fits this framework. The TO couples mathematical optimization algorithms to Finite Elements Analysis (FEA) to suggest structural design outcomes ensuring an optimal material distribution within a given reference domain. Specified optimization objectives, design constraints, loads, and boundary conditions are applied to the study case [6]. Stresses, displacements, natural frequencies, and geometrical features

are typically encompassed as design constraints towards the achievement of an optimal solution, although they can also be included as the TO objectives to be pursued within the optimization iterations [7].

Since the optimal material distribution may lead to complex geometry, the TO outcomes can become ready-made Additive Manufacturing (AM) designs. Alternatively, a further post-processing stage can be introduced to adapt the design for traditional—material subtractive—manufacturing techniques. Nevertheless, this strategy allows to bypass the time-consuming engineering and iterative design mechanisms, as the optimal solution coincides with the outcome of the process itself. The TO is rapidly widespread in aerospace components design and improvement, and a multitude of examples can be retrieved in the literature [8,9]. Worth mentioning are the VEGA launcher connector support [10], a structural component obtained via a frequency-driven TO, or the Airbus A320 nacelle hinge bracket [11], an aircraft part manufactured exploiting Additive Layer Manufacturing (ALM) after its optimization. Another significant example is the antenna support for the ESA Sentinel 1 satellite [12,13], a component redesigned exploiting TO towards the achievement of mass minimization and finally manufactured via Selective Laser Sintering (SLS).

This research work extensively describes the MicroMED Dust Analyzer Optical Bench (OB) TO-driven redesign workflow and results assessment activities. The instrument is an amplitude-dependent single Optical Particle Counter (OPC) designed and qualified for the ESA ExoMars 2022 mission towards Mars [14–16]. The instrument includes several subassemblies and hardware components arranged in a compact and lightweight design, whose locations are depicted in Figure 1 and was intended to infer the airborne dust size and size distribution in situ at the lowest troposphere of the Red Planet [17–19]. This would be a groundbreaking achievement because, at present, data about dust on Mars were exclusively acquired using remote sensing (e.g., thermal IR instruments, near-IR spectrometers, and Terrestrial ground-based telescopes).

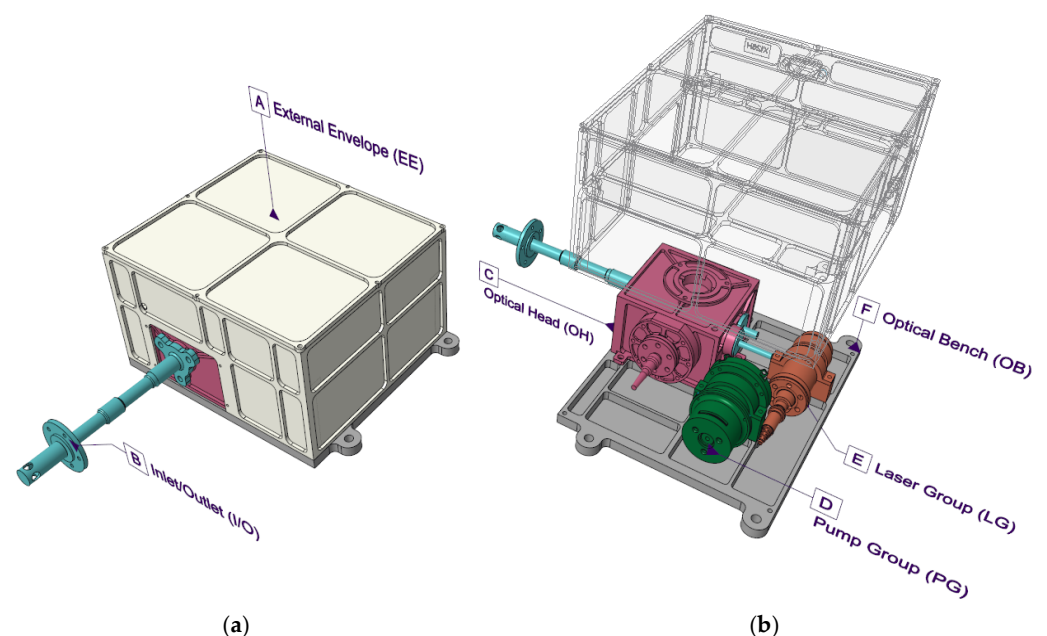


Figure 1. MicroMED Dust Analyzer model overview (a) and exploded view (b). The main sub-assemblies are highlighted: A. External Envelope; B. Inlet/Outlet; C. Optical Head; D. Pump Group; E. Laser Group; F. Optical Bench.

A proper fluidic system was designed to suction the Martian aerosol—a multiphase mixture of gases and solid dust particles—and transfer it to the MicroMED Optical Head (OH). There, the fines are investigated by a collimated low-power NIR laser beam (having a

single-mode nominal optical power of 150 mW and a lasing wavelength of 830 ± 5 nm) and finally returned to the Martian environment. The scattered light produced by the interaction between the particles and the laser is conveyed by a parabolic mirror towards a photodiode detector, responsible for the particle size measurements. MicroMED functional components and subassemblies are mounted on the OB and shielded from the harsh Martian land by the External Envelope (EE) [20–22].

The activities described in the following aim to complete the redesign work aiming to obtain two different optimal OB design proposals with an improved performance. The feasibility design was successfully carried out by the author in [23], but the numerical investigation has been extended, focusing on the evaluation of the thermo-elastic behaviour of the proposed solutions in the worst-case temperature. Moreover, the experimental assessment of the modal behaviour of a mockup of one of the two optimal solutions is presented, aiming to validate the presented methodology and related results.

The added value of this research work lies in the innovative approach adopted for the OB improvement. The latter is presented in Section 2 along with the FEA procedure involved within the parts' numerical assessment, whose results are summarized in Section 3. The achievements consist of optimal design proposals to improve the current—suboptimal—material arrangement within the OB. Starting from the achieved design proposals, as a further improvement of the research activity a mockup of the lightened OB was manufactured and tested to prove the effectiveness of the TO design. Finally, the experimental validation campaign is presented in Section 4, comparing the outcomes with the numerical ones and completing the OB optimization activity.

2. Materials and Methods

The MicroMED OB is the support plate on which the instrument subassemblies and functional components are firmly fixed. The OB is a ribbed aluminum component (i.e., manufactured in Al7075-T6 aluminum alloy) characterized by high mechanical stiffness, provided by the grid of ribs lying on its interface plate. In this research work, the main investigation dealt with the topology and sizing of the OB ribs, pursuing the optimal configuration towards mass minimization achievement (i.e., hereafter referred to as Model A) maintaining comparable dynamic performance with respect to the current OB design. Furthermore, a different layout was probed, aiming to optimize the OB dynamic performance (i.e., hereafter referred to as Model B). The latter proposal was obtained by maintaining the unchanged mass budget allocated to the ribs grid while maximizing the OB resonance frequencies.

The TO method was preferred to the other structural optimization approaches, i.e., the size and the shape optimization methods, because of its design freedom. Both Model A and Model B redesign studies exploited two commercial software programs, i.e., PTC Creo Parametric/Simulate and Altair Inspire. The former was adopted for computer-aided modelling and FEAs, while the latter was employed for the TO. A schematic of the workflow exploited for the redesign is depicted in Figure 2.

Within the optimization process, Altair Inspire relies on a computational method based on the material distribution technique. This process adopts the material density as the design variable and returns an optimal material distribution in a discretized reference domain [24,25]. A binary solid model is produced, and for each reference domain finite element either a unitary or null value is assigned to the design variable. Consequently, a finite element will be finally part of the optimal structure only if its associated design variable has a non-null value. In the latter case, the material density is assigned to the finite element. The software engine, to cope with the occurrence of the intermediate values of the design value (i.e., between 0 and 1) during the optimization iterations, adopts a penalization approach based on the Solid Isotropic Material with Penalization (SIMP) algorithm [26,27]. Therefore, the outcome will be composed of either voids or solids.

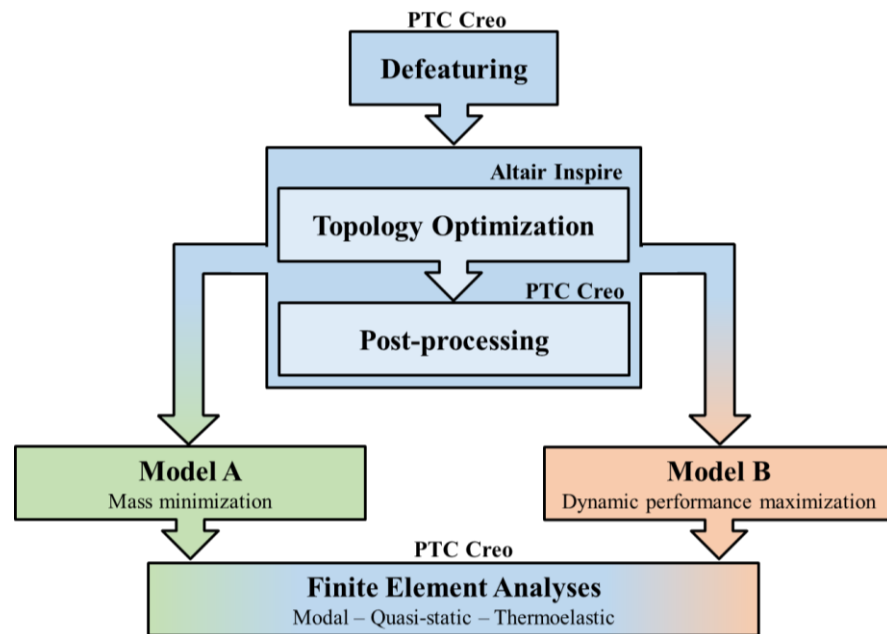


Figure 2. Block chart of the phases included within the OB redesign and optimization workflow.

In this research work, the optimization cycles imposed the finite element structure mechanical stiffness maximization as the design target. At the beginning of each iteration, the overall mass of the reference domain was progressively reduced by a percentage within the total reference domain volume. For the OB optimization, at the beginning of each TO step, 70% of the design volume removed was imposed as an output condition. Before running the optimizations, a filled OB solid model was developed, as depicted in Figure 3. Solid model defeaturing was carried out as the first task to reduce the computational complexity of the FEAs, while maintaining the representativeness of the numerical outcomes.

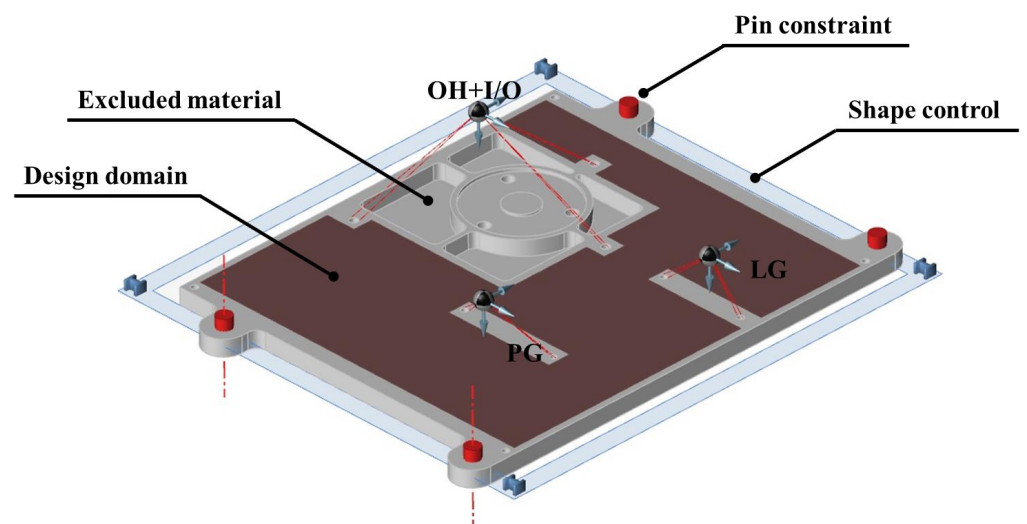


Figure 3. Altair Inspire TO model of the OB. The brown region represents the design domain subject to the SIMP approach and the grey one was left unaltered during the optimization iterations.

The Finite Element Model (FEM) held three lumped masses connected via rigid links to the OB areas intended to support the instrument subassemblies. Such areas were excluded from the design domain and thus were not involved in the optimization cycles. These features—92 g for the OH + Inlet/Outlet (IO), 51 g for the Pump Group (PG), and 29 g for the Laser Group (LG)—were introduced to consider the main instrument’s subassemblies

but in the meantime to run a streamlined optimization process. The lumped masses were estimated by assigning the aluminum density (i.e., 2819 kg/m^3) and assuming a 10% margin as the worst-case scenario. The material depletion of the design domain (Figure 3), i.e., the only region eligible for the TO, was performed by generating constant height ribs in the direction perpendicular to the OB floor. No voids nor holes throughout the height of the ribs were allowed for the final design.

The loading condition applied for the optimization was a quasi-static acceleration of 1000 m/s^2 on each lumped mass, in each direction. Each iteration for Model A concluded only when the result produced a new model having the first natural frequency fulfilling the design dynamic requirement, thus when the first three resonances were equal or larger than the current OB ones. On the other hand, for the Model B development, the optimization was interrupted only when the optimal material distribution was identified, i.e., the one providing the highest value possible for the component's natural frequencies. In this case, the design constraint was set on the mass budget spent on the ribs grid, imposed equal to the current OB one. Moreover, as pointed out in Figure 2, following the TO, a post-processing activity was performed on the optimal solutions, with the aim of smoothing and homogenizing the optimal ribs grid towards a milling/Electrical Discharge Machining (EDM) manufacturing process. Preliminarily, a FEM of the current OB was developed in PTC Creo Parametric/Simulate environment to define the baseline performance to be exploited during the TO. As shown in Figure 4, pin constraints were placed at the OB peripheral holes to simulate the MicroMED instrument mounting interface on the Dust Suite, the ESA ExoMars 2022 lander surface platform. Mesh refinement was applied to the FEM, obtaining an overall of 32,371 finite elements, split between 28,704 solid tetrahedrons and 3667 shell triangles. Likewise, the FEMs for the optimal and post-processed OBs were developed. The performance of the models was estimated relying on the FEAs set:

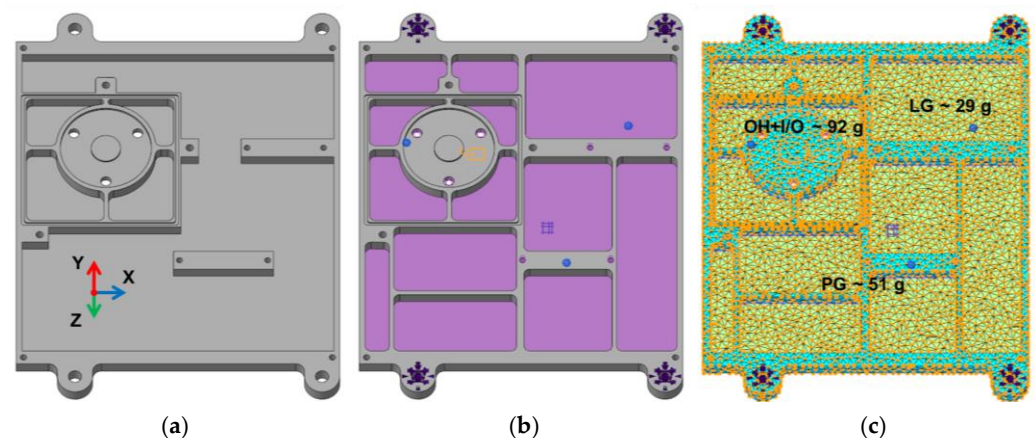


Figure 4. OB model without (a) and with (b) the stiffening ribs grid. FEAs features (i.e., lumped masses, rigid links, shells, and constraints) are highlighted. The mesh was applied to the model (c).

- Modal analysis aiming to estimate the first five natural frequencies;
- Quasi-static analyses applying a load of 1000 m/s^2 , probing the state of stress distribution of the models considering three different loading directions (i.e., X, Y, and Z according to the reference frame reported in Figure 4) and resembling the excitation expected during the takeoff and landing phases of the mission; and
- Thermoelastic analyses in either non-operational (i.e., the cold case, considering a temperature shift from the reference $+20 \text{ }^\circ\text{C}$ to the target $-40 \text{ }^\circ\text{C}$) or operational (i.e., the hot case, likewise the cold case but within the range $+20 \text{ }^\circ\text{C}$ and $+40 \text{ }^\circ\text{C}$) conditions.

The figure of merit to state the quasi-static and thermoelastic FEAs goodness was the Margin of Safety (*MoS*). The *MoS* was evaluated to highlight the resistance of the

mechanical component during the assessments, relying on the Von Mises yield criterion for ductile materials. The *MoS* was computed referring to the following formulation:

$$MoS = \frac{\sigma_{YS}}{\eta \cdot \sigma_{VM}} - 1 \quad (1)$$

In the equation, σ_{YS} was the material yielding stress (i.e., 503 MPa for the Al7075-T6), η was the admissible safety factor (i.e., 1.5 as reported in the ECSS-E-ST-33-01C design standard [28]), and σ_{VM} was the maximum Von Mises stress resulting from the simulation. The assessment was considered satisfactory with positive *MoS*.

Moreover, the thermal deformations induced within the temperature ranges were probed both for the current and the optimal OBs. The intent was to quantify the impact of the temperature on the structural stability of the MicroMED hardware, i.e., estimating the misalignment between the laser light and the aerosol flux due to the thermal deformations of the mechanical parts for the cold and hot cases. As depicted in Figure 5, the OH was assembled with the OB; on the former, the Laser Delivery Group (LDG, composed of the 213 and 11B parts) was fastened, as well as the IO, which was split between the Inlet Tube (IT, composed by the 022 and 026 parts) and the Exhaust Tube (ET, or the 023 part). A cloud of probes to measure the displacements along the X, Y, and Z axes was introduced at the LDG, IT, and ET extremities facing the sampling volume inside the OH. The relative shift among the probes allowed for an estimation of the misalignment at the instrument sampling volume. According to its magnitude, the latter can produce a negative impact on the MicroMED performance, jeopardizing the particle size identification and increasing the overall measurement uncertainty.

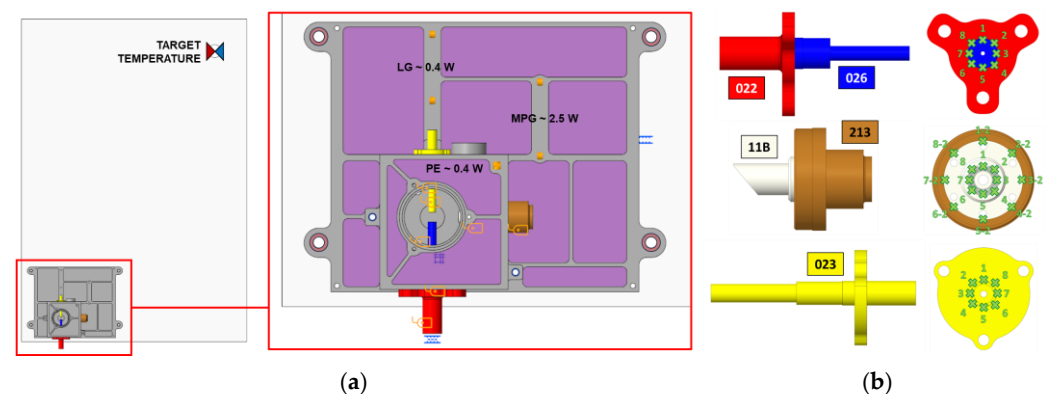


Figure 5. FEM for the thermal deformations quantification (a) and detail on the positions of the probes (b). The included dissipated thermal powers are of the Proximity Electronics (PE), the Laser Group (LG), and the Motor Pump Group (MPG), respectively.

3. Results

In this section, the OB redesign outcomes are presented and discussed. The results of the FEAs are outlined in the following firstly for the current OB preliminary investigation, then for the Model A and Model B proposals.

3.1. Current OB

The MicroMED current OB was manufactured with the Al7075-T6 aluminium alloy, leading to a mass budget of about 68.5 g. The material allocated to the ribs grid—which is the one eligible to be reduced—was estimated to be about 7 g (i.e., approximately 10% of the OB mass).

The results of the performed FEAs set are summarized in Table 1 and the most critical loading conditions (i.e., 1000 m/s² acceleration along the Y-axis for the quasi-static analysis and the cold case for thermoelastic stresses) are reported in Figure 6. The numerical investigation pointed out that the current OB's first natural frequency was about 407 Hz.

Moreover, the maximum Von Mises stress arising for the quasi-static and thermoelastic analyses was approximately 84 MPa and 12 MPa, respectively. A largely positive *MoS* of about 3 and 28 was obtained for the former and the latter case studies.

Table 1. MicroMED current OB FEAs outcomes.

Resonances [Hz]					Von Mises Quasi-Static Stresses [MPa]					
f_1	f_2	f_3	f_4	f_5	σ_X	<i>MoS</i>	σ_Y	<i>MoS</i>	σ_Z	<i>MoS</i>
407	530	798	926	1193	29	10.7	84	2.99	45	6.50
Von Mises Thermoelastic Stresses [MPa]										
Cold case				<i>MoS</i>			Hot case		<i>MoS</i>	
12				28			4		88	

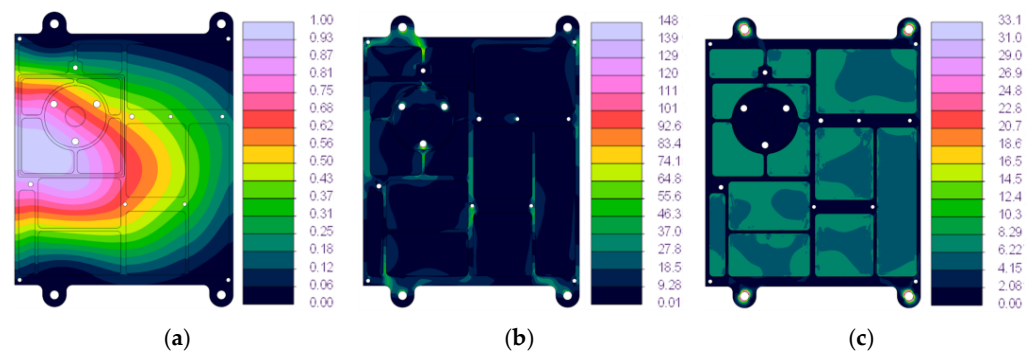


Figure 6. MicroMED current OB first resonance mode shape (a); Von Mises stress distribution [MPa] with 1000 m/s² load in Y direction (b) and thermoelastic cold case (c).

Finally, the thermal deformations estimated within the sampling volume in the OH are reported. The results are shown for both the cold case and the hot case in Figure 7, completing the preliminary activities for the baseline identification. As can be noticed, no significant relative displacement was highlighted, suggesting the thermal stability of the current OB assembly. Indeed, a maximum relative displacement of about 2.1 μm and 710 nm was computed, values which are three orders of magnitude smaller than the sampling volume ellipse major axis (i.e., about 1 mm) obtained crossing the laser beam with the multiphase flow in the OH. The displacements measured at the probes in the three directions with respect to the reference frame XYZ are reported in Appendix B.

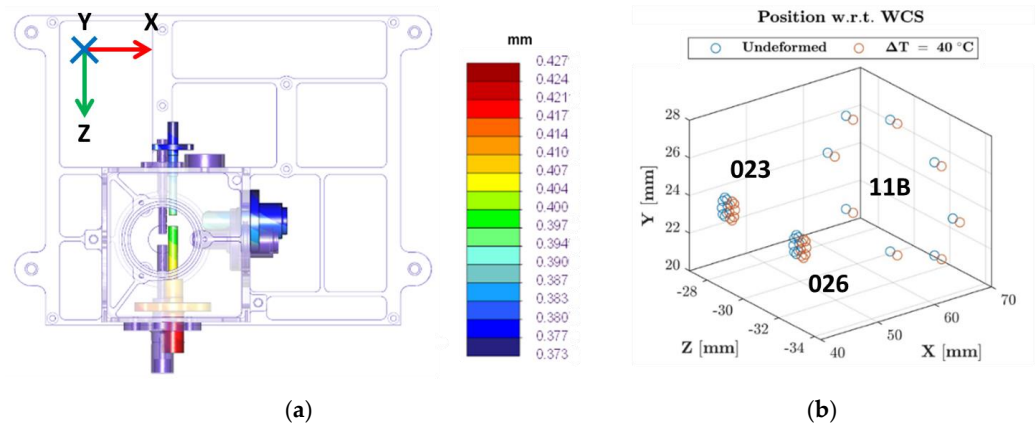


Figure 7. Overview of MicroMED current OB assembly relative thermal deformations for the cold case (a) and displacements at the defined probes (b).

3.2. Optimal OB—Model A

The rough optimal solution to be post-processed was obtained through three iterative TO cycles, whose outcomes are presented in Figure 8. The overall computational time required for completing the optimization was about 48 h, using an Intel®Core™ i7-12700H processor. On the other hand, the definitive Model A design is depicted in Figure 9. Assigning Al7075-T6 as material (i.e., having a density of about 2810 kg/m³) a mass of 64.63 g was estimated, of which 3.18 g were allocated to the ribs grid.

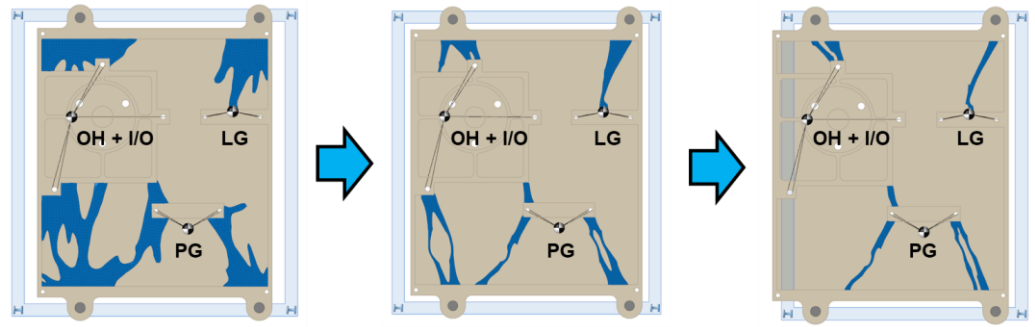


Figure 8. TO iterative cycles results (blue colour) for the Model A.

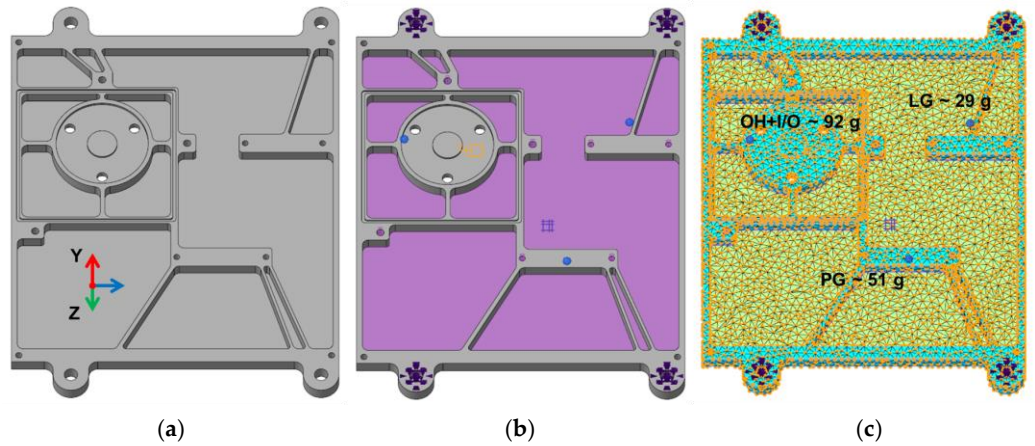


Figure 9. Model A without (a) and with (b) the stiffening ribs grid. FEAs features (i.e., lumped masses, rigid links, shells, and constraints) are highlighted. The mesh was applied to the model (c).

For the Model A, the FEM comprised 32,042 finite elements, split between 28,282 solid tetrahedrons and 3767 shell triangles. The FEAs results are summarized in Table 2, while the most critical loading conditions (i.e., 1000 m/s² acceleration along the Y-axis for the quasi-static analysis and the cold case for thermoelastic stresses) are reported in Figure 10. In particular, a first natural frequency of about 412 Hz was estimated, while a maximum Von Mises stress of 107 MPa (i.e., leading to a *MoS* of 2.12) and 11 MPa (i.e., leading to a *MoS* of 29) was found for the quasi-static and the thermoelastic analyses, respectively.

Table 2. MicroMED Model A OB FEAs outcomes.

Resonances [Hz]					Von Mises Quasi-Static Stresses [MPa]					
f_1	f_2	f_3	f_4	f_5	σ_X	<i>MoS</i>	σ_Y	<i>MoS</i>	σ_Z	<i>MoS</i>
412	521	627	745	791	39	7.50	107	2.12	50	5.74
Von Mises Thermoelastic Stresses [MPa]										
Cold case			<i>MoS</i>		Hot case			<i>MoS</i>		
11			29		4			88		

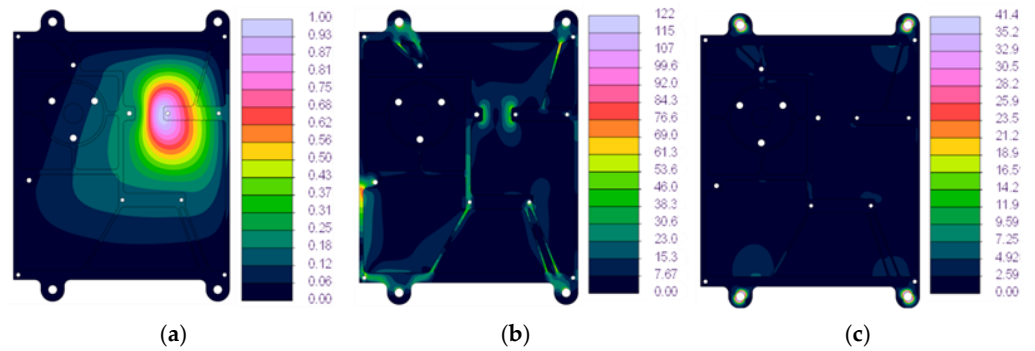


Figure 10. MicroMED Model A first resonance mode shape (a); Von Mises stress distribution [MPa] with 1000 m/s² load in Y direction (b) and thermoelastic cold case (c).

The thermal deformations are reported in Figure 11. Negligible relative displacements were obtained (i.e., 581 nm and 499 nm for the cold case and hot case, respectively), validating the thermo-mechanical behaviour of the proposed solution. The displacements measured at the probes in the three directions with respect to the reference frame XYZ are reported in Appendix B.

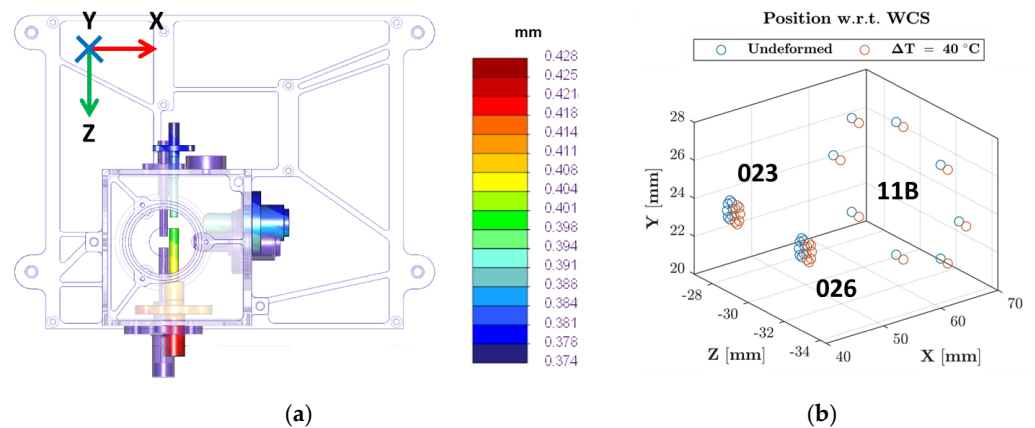


Figure 11. Overview of MicroMED Model A assembly relative thermal deformations for the cold case (a) and displacements at the defined probes (b).

3.3. Optimal OB-Model B

The rough optimal solution was obtained via three TO iterations, whose outcomes are reported in Figure 12. The Model B final design proposal is depicted in Figure 13.

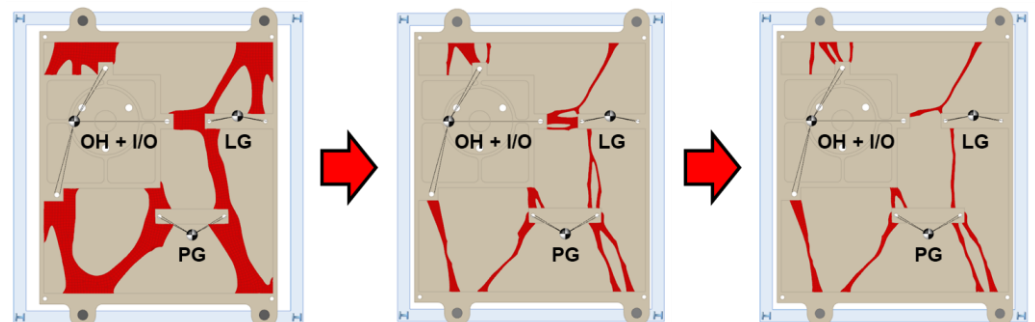


Figure 12. TO iterative cycles results (red colour) for the Model B.

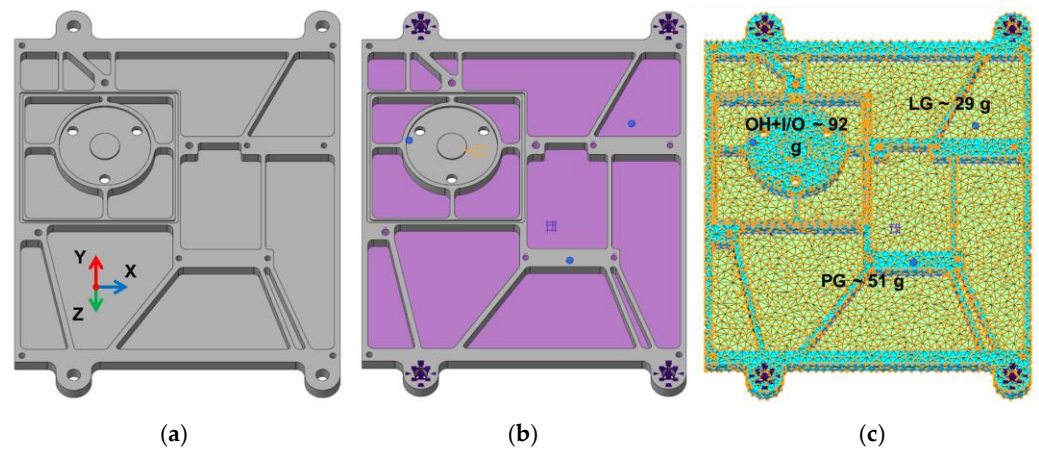


Figure 13. Model B without (a) and with (b) the stiffening ribs grid. FEAs features (i.e., lumped masses, rigid links, shells, and constraints) are highlighted. The mesh was applied to the model (c).

The optimization process took an overall computational time comparable with the Model A design process. For the Model B, the FEM comprised 32,999 finite elements, split between 29,240 solid tetrahedrons and 3759 shell triangles. The FEAs results are summarized in Table 3, while the most critical loading conditions (i.e., 1000 m/s² acceleration along the Y-axis for the quasi-static analysis and the cold case for thermoelastic stresses) are reported in Figure 14.

Table 3. MicroMED Model B OB FEAs outcomes.

Resonances [Hz]					Von Mises Quasi-Static Stresses [MPa]					
f ₁	f ₂	f ₃	f ₄	f ₅	σ _X	MoS	σ _Y	MoS	σ _Z	MoS
607	725	872	1104	1240	25	12.6	87	2.86	34	8.85
Von Mises Thermoelastic Stresses [MPa]										
Cold case				MoS			Hot case		MoS	
31				9.9			10		31.7	

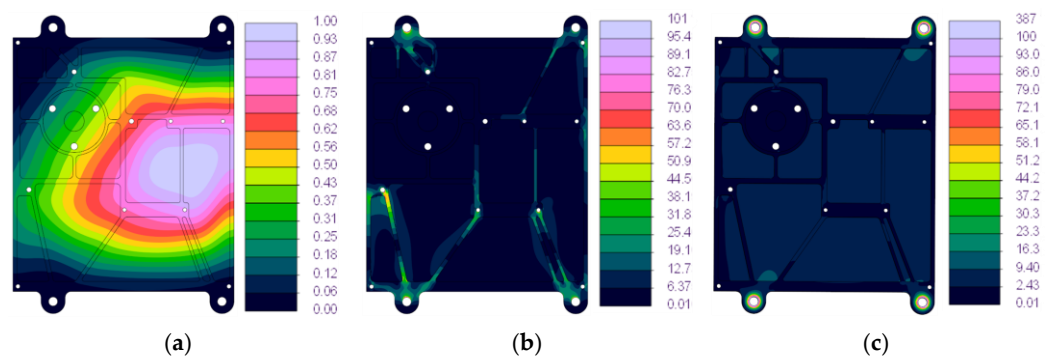


Figure 14. MicroMED Model B first resonance mode shape (a); Von Mises stress distribution [MPa] with 1000 m/s² load in Y direction (b) and thermoelastic cold case (c).

In particular, a first natural frequency of about 607 Hz was estimated, while a maximum Von Mises stress of 87 MPa (i.e., leading to a MoS of 2.86) and 31 MPa (i.e., leading to a MoS of 9.9) was found for the quasi-static and the thermoelastic analyses, respectively. The thermal deformation is reported in Figure 15. Negligible relative displacements were obtained for the model B design (i.e., 761 nm and 752 nm for the cold case and hot case, respectively). The displacements measured at the probes in the three directions with respect to the reference frame XYZ are reported in Appendix B.

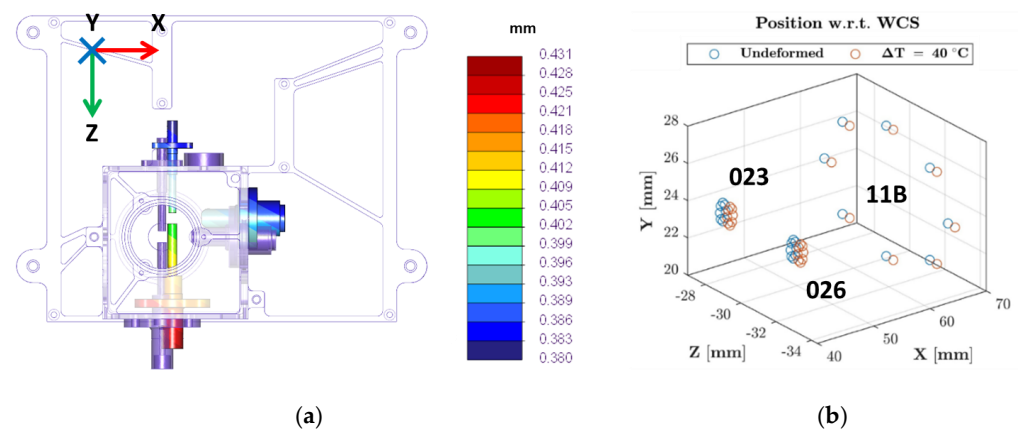


Figure 15. Overview of MicroMED Model B assembly relative thermal deformations for the cold case (a) and displacements at the defined probes (b).

3.4. Optimizations Findings Discussion

The numerical results showed that the first natural frequency of the current OB was about 407 Hz. As depicted in Figure 6, the corresponding mode shape included an alternate bending of the OB produced by the heavy OH lumped mass on its footprint. The motion slightly involved the MPG and LG subassemblies as well. Moreover, the quasi-static analyses pointed out that the worst loading case was the one encompassing the 1000 m/s^2 acceleration along the Y-axis. This was attributed to the larger mechanical compliance of the OB in the latter direction with respect to the others. Finally, the cold case and the hot case analyses suggested that for both the foreseen temperature ranges fully compliant stress values were achieved, and negligible thermal deformations as well.

With the Model A proposal, the TO guaranteed a mass budget of 64.63 g. The mass saving was approximately 55% of the mass allocated to the ribs grid (i.e., 3.18 g against about 7 g of the current OB), corresponding to approximately 6% of the overall component mass. The modal analyses highlighted that the Model A first natural frequency was at about 412 Hz, i.e., a value comparable with the current OB one. Moreover, comparing Figure 6 with Figure 10, a change in the mode shape can be noticed: the first natural frequency mode shape involved mainly the LG, a favorable condition considering the motion is displaced from the OH footprint, i.e., the most sensible region of MicroMED to preserve the alignment of the instrument. In addition, all the quasi-static and thermoelastic analyses provided positive safety margins, proving the effectiveness and robustness of the proposed design.

Similarly, the numerical results achieved with the Model B were promising. Indeed, the modal analysis showed that the optimal component natural frequencies were taking place at values larger than the current OB ones. In particular, the first natural frequency was at about 607 Hz, corresponding to an increase of approximately 50% with respect to the current OB one while maintaining a comparable mass budget. Likewise, the Model A, the mode shape was slightly shifted towards the LG footprint (Figure 14). Moreover, the quasi-static analyses and the thermoelastic analyses provided a decrease of the Von Mises stresses magnitude for the former and a slight increase for the latter. The result was explained considering that Model B has larger mechanical stiffness with respect to the current OB, therefore providing increased structural robustness of the component and reduced thermal compliance.

Finally, both Model A and B highlighted negligible thermal deformations for the investigated case study, showing that the proposed designs are not sensible to the temperature environment foreseen by the mission.

Indeed, among the proposed designs, both providing interesting improvements with respect to the current configuration, Model A was considered the most promising one for MicroMED mechanical hardware future development and was selected for further experimental investigation.

4. Experimental Assessment

As mentioned before, mass minimization plays a key role in aerospace components design. In this light, among the proposals probed within this research work, Model A was considered the most promising one for MicroMED mechanical hardware future development. Despite the optimal OB robustness being positively proven numerically via FEAs, for completing the circle an experimental activity to further freeze the adopted workflow was carried out. Indeed, a mockup of the Model A was manufactured by milling from an Al7075-T6 slab (Figure 16) and was tested to measure the free natural frequencies. Before the experimental testing activities, a dimensional and geometrical check was performed to state the actual mockup footprint, to update the FEM.

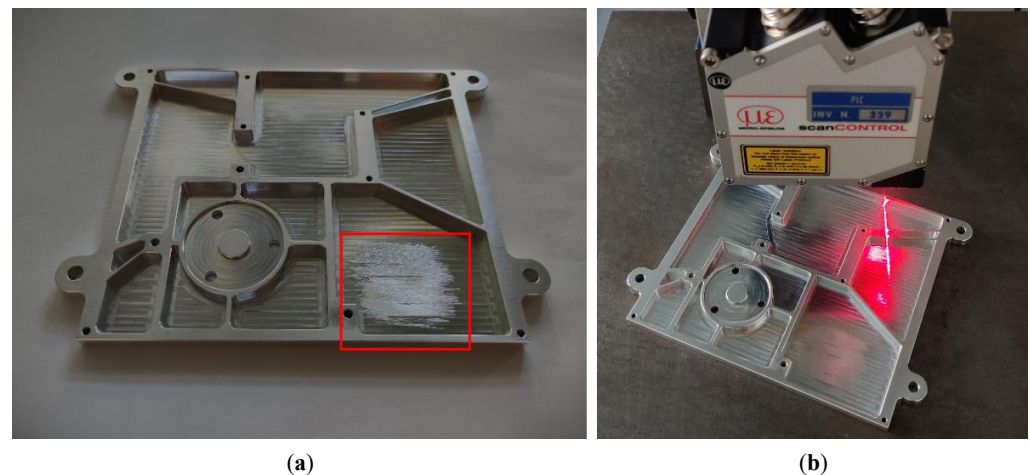


Figure 16. Manufactured Model A mockup highlighting the damaged region (in the red box) (a) and the laser scanner measurement setup (b).

The mass was measured with a Gibertini balance having a resolution of 0.01 g, obtaining 63.88 g. The mass mismatch with the Model A Computer-Aided Design (CAD) was attributed to a slight difference between the real and theoretical component dimensions. Indeed, a measure of the ribs grid and the overall OB geometrical features—carried out with a Mitutoyo fiftieths gauge and a Micro-Epsilon laser scanner having a resolution of 2 μm —confirmed the presence of a dimensional unevenness. The measurement outcome is reported in Appendix A, providing a comparison between the theoretical and real dimensions of Model A.

The activity was propaedeutic to the actual free vibrations test because it allowed updating the Model A CAD model with the real mockup dimensions and preserving its representativeness. This was mandatory in view of a comparison between the numerical free natural frequencies (i.e., found running a free modal analysis on PTC Creo Parametric/Simulate) with the experimental one.

Moreover, as highlighted in Figure 16 during the manufacturing process the 0.3 mm skin was not able to withstand the milling head-cutting force and was plastically deformed by the tool action. However, since the damage was localized to a restricted area of the component, the mockup was considered eligible to be investigated in this experimental activity. Indeed, its structural integrity was not compromised and the vibrating modes not involving the damaged region were expected to be unaffected by the manufacturing defect.

Finally, before the actual resonances research experimental activity, the Model A updated CAD was subject to a free modal analysis to estimate the free natural frequencies and discover which vibrating modes were eligible to be observed during the resonances research. Indeed, considering a non-contact measurement method including a Laser Doppler Vibrometer (LDV—Polytec OFV 505 sensor head) was used for the experimental activity, the free modal analysis was necessary to plan where to point the laser head to properly catch the vibrating modes and measure their frequencies.

The FEA outcomes are reported in Figure 17 and the numerical results are summarized in Table 4. As can be seen, with only three LDV laser spot positionings (i.e., at one of the peripheral mockup holes, at the skin between the LG and the PG, and near the component damaged area) it was theoretically possible to catch all the investigated vibrating modes.

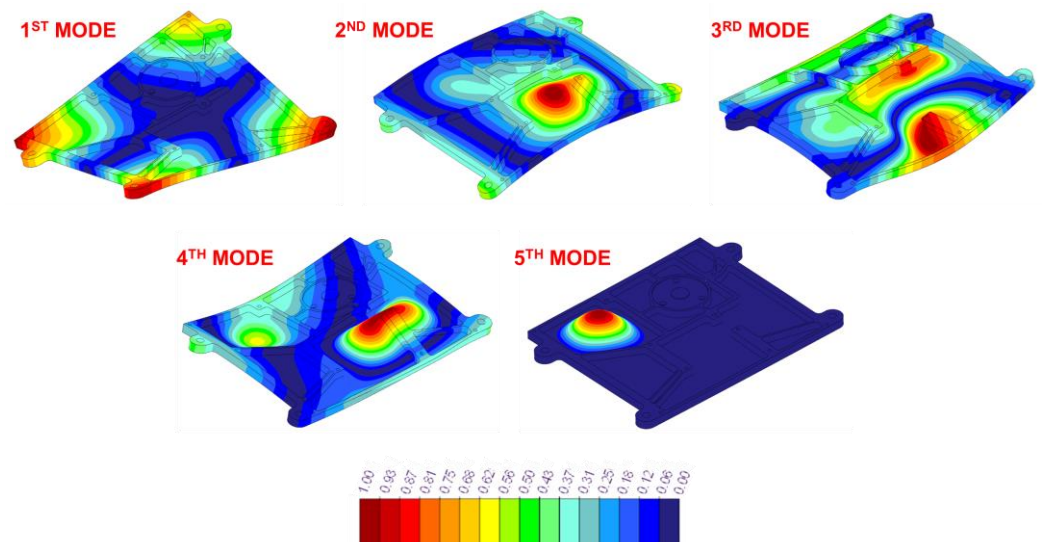


Figure 17. Model A mockup modal analysis, vibrating modes.

Table 4. Numerical free vibrating modes summary carried out on the Model A updated CAD. In the brackets, the numerical free vibrating modes before the update are reported.

Natural Vibrating Resonances [Hz]					
f_1	f_2	f_3	f_4	f_5	
392	747	898	990	1159	
(390)	(742)	(904)	(991)	(1168)	

An overview of the adopted experimental setup is depicted in Figure 18. For the free vibrations test, the Model A mockup was suspended on elastic ropes and excited with a series of sweep sines (i.e., five consecutive linear sweeps lasting 30 s each, in the 80 to 5120 Hz frequency range and 200 mV peak-to-peak wide) produced by the Keysight Technologies 33220A function generator and delivered to a loudspeaker placed below the OB. The real input delivered at the mockup was measured with the PCB Piezotronics 130E20 ICP microphone (i.e., having a sensitivity of 48.1 mV/Pa). On the other hand, the mockup response was measured relying on the LDV (i.e., having a sensitivity of 40 mV/(mm/s) and a band-pass filter between 100 Hz and 10 kHz) and sampled at 10,240 Hz via the National Instrument NI 9234 acquisition board (i.e., characterized by an input range of ± 5 V and 24 bit). The LDV beam was pointed at three strategic positions within the Model A mockup according to the free natural frequencies mode shapes identified via the free modal analysis. Finally, the experimental free natural frequencies were estimated relying on the Frequency Response Function (FRF) computed with the ratio between the LDV and the microphone signals, windowing (Hanning) and averaging the acquired time histories. Results are shown in Figure 19.

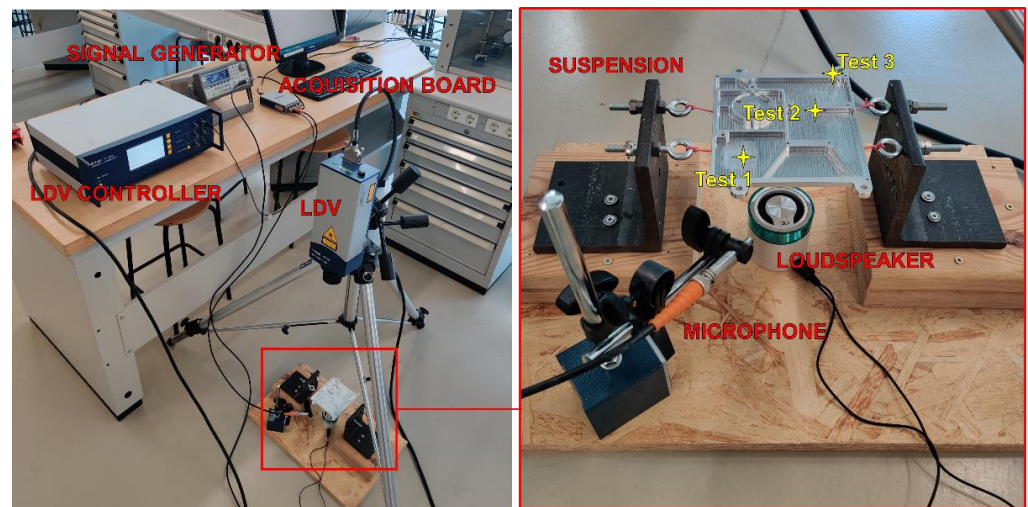


Figure 18. Model A mockup free modal testing setup.

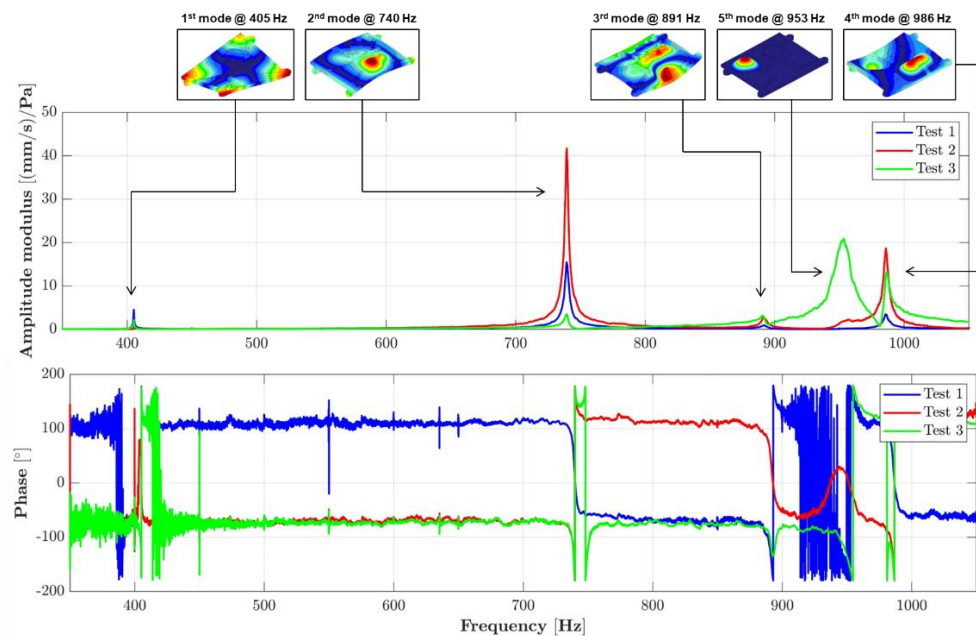


Figure 19. Measured FRFs for the Model A mockup.

A comparison between numerical and experimental natural frequency values is reported in Table 5. As can be seen, all the investigated resonances—but the 5th—are in line with the numerical ones, i.e., the retrieved error is smaller than 5%. The discrepancy between the numerical and the experimental natural frequency value at the 5th vibrating mode was explained considering observing the mode shape reported in Figure 17. Indeed, the considered mode exclusively involved the thin skin affected by the manufacturing damage pointed out in Figure 16. Therefore, such local weakening may have sensibly reduced the component stiffness there and caused the natural frequency value to drop.

Nevertheless, in light of the satisfactory results with the comparison, the validation activity to state the robustness of the redesign approach was considered positive.

Table 5. Comparison between the numerical and the experimental natural frequency values.

Vibrating Mode	Numerical [Hz]	Experimental [Hz]	Δ
1st	392	405	+3.32%
2nd	747	740	−1.00%
3rd	898	891	−0.74%
4th	990	986	−0.42%
5th	1159	953	−17.8%

5. Conclusions

This research work proposed the redesign of the optical bench for the MicroMED Dust Analyzer, an OPC developed for the ESA ExoMars 2022 mission to Mars. Topology optimization was exploited to achieve either a mass saving on the component (i.e., Model A) or a maximization of its dynamic performance (i.e., Model B). The optimal proposals allowed a reduction of about 55% of the mass budget of the considered design domain, or a first natural frequency improvement of about 50% than the current optical bench design. Both of the solutions were positively assessed via a set of FEAs (i.e., modal, quasi-static, and thermoelastic analyses) applying the conditions identified as design constraints within the mission framework and highlighting large safety factors about the limit stress for both the foreseen mechanical and thermal environment. Moreover, the thermo-elastic analyses showed that computed thermal deformation is negligible with respect to the instrument's measurement volume size, therefore validating the thermo-mechanical structural design.

The Model A was considered the most promising proposal for the MicroMED future development. Indeed, applying the mass reduction to the overall instrument is foreseen to provide the largest benefit to MicroMED. Any additional mass saving among the mechanical hardware would allow either the possibility of proposing a cost-competitive instrument, or a redistribution of the gained mass elsewhere to enhance the functionalities of the instrument. Considering the latter option, one very attractive feature would be the possibility to quickly and easily dismount or replace the instrument components even after the integration is completed.

Considering the attractiveness of the Model A proposal, a mockup of the optical bench was manufactured and tested to prove the robustness of the redesign workflow as well. An experimental setup was put in place to measure the mockup-free natural frequencies, obtaining a good agreement with the ones predicted via a numerical free modal analysis, i.e., a percentage error lower than 5% was found for the first four natural frequencies.

Nevertheless, both Model A and Model B proved the effectiveness of the adopted structural optimization approach. Thus, as this research activity develops in the future, the redesign methodology will be extended to the main mechanical components of the instrument.

Author Contributions: Conceptualization, M.G.C. and D.S.; methodology, M.G.C., B.S. and D.S.; validation, M.G.C., B.S., F.E., G.F., C.P., G.M., F.C. and D.S.; formal analysis, M.G.C., B.S. and D.S.; investigation, M.G.C., B.S., F.E., G.F., C.P., G.M., F.C. and D.S.; writing—original draft preparation, M.G.C.; writing—review and editing B.S., F.E., G.F., C.P., G.M., F.C. and D.S.; supervision, D.S.; funding acquisition, B.S. and F.E. All authors have read and agreed to the published version of the manuscript.

Funding: This research was funded by the Italian Space Agency (ASI) with the contract ASI-INAF n. 2023-3-HH.0, project name “Attività Scientifica di Preparazione all’Esplorazione Marziana” CUP F83C23000030005.

Institutional Review Board Statement: Not applicable.

Informed Consent Statement: Not applicable.

Data Availability Statement: Data are contained within the article.

Conflicts of Interest: The authors declare no conflict of interest.

Appendix A

The Model A was subject to a geometrical and dimensional check to state the real footprint with respect to the FEM one. The measurements were carried out at the positions highlighted in Figure A1. Finally, the campaign outcomes are summarized in Table A1.

Table A1. Summary of the dimensional measurements—with reference to Figure A1—carried out on the Model A manufactured mockup.

Fiftieths Linear Gauge (RES 0.02 mm)			Laser Scanner (RES 0.002 mm)		
Model A footprint: 110.04 × 125.98 mm			Ref.	Measured [mm]	Nominal [mm]
Gibertini balance (RES 0.01 g)			R1	1.484	1.500
Measured mass [g]	Nominal mass [g]		R2	0.988	1.000
63.88	64.63		R3	1.002	1.000
Mitutoyo micrometer (RES 0.001 mm)			R4	1.192	1.200
Ref.	Measured [mm]	Nominal [mm]	R5	1.940	2.000
S1	0.289	0.300	R6	0.984	1.000
S2	0.283	0.300	R7	1.466	1.500
S3	0.282	0.300	R8	1.480	1.500
S4	0.284	0.300	R9	1.464	1.500
S5	0.287	0.300	Fiftieths linear gauge (RES 0.02 mm)		
S6	0.288	0.300	Ref.	Measured [mm]	Nominal [mm]
S7	0.289	0.300	T1	5.00	5.00
S8	0.283	0.300	T2	2.44	2.50
S9	0.282	0.300	T3	2.44	2.50
S10	0.284	0.300	T4	3.50	3.50
H1	0.287	5.000	T5	7.00	7.00
H2	0.288	5.000	T6	3.44	3.50
H3	0.292	5.000	T7	4.94	5.00
H4	0.283	5.000	T8	1.92	2.00
H5	0.285	5.000	T9	1.94	2.00
H6	0.284	5.000	T10	6.96	7.00

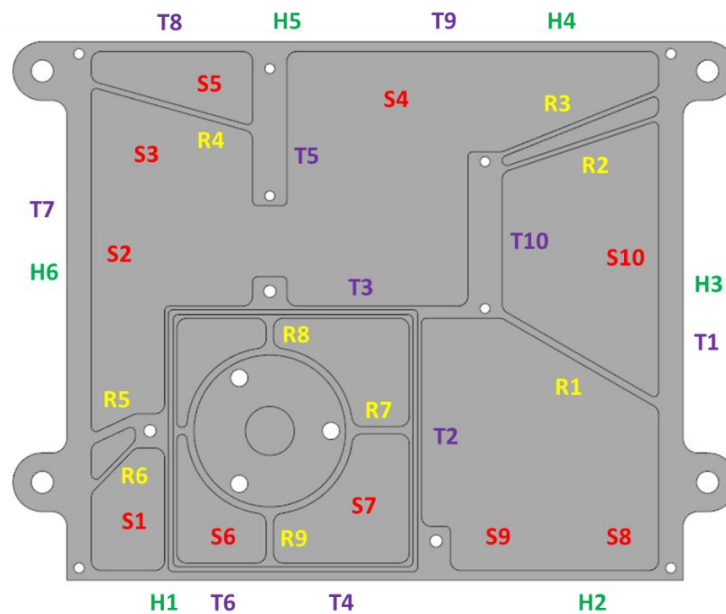


Figure A1. Overview of the measurement points positioning at the Model A mockup. The tags with the *T* prefix refer to general thickness measurements; *R* prefix refers to rib thickness measurements; *S* prefix refers to skin thickness measurements; and *H* refers to features height measurements.

Appendix B

The displacements produced at the probes defined in Figure 5 are reported—for the most critical case, i.e., the cold case—in Table A1. The numerical values for the current OB, Model A, and Model B were estimated relying on an FEA and considering singularly the X, Y, and Z directions.

Table A1. Summary of the thermal deformations obtained within the cold case for the three FEM of the MicroMED OB.

Probe ID	Displacement with Respect to the Initial Probe Coordinates								
	Current OB			Model A			Model B		
	X [mm]	Y [mm]	Z [mm]	X [mm]	Y [mm]	Z [mm]	X [mm]	Y [mm]	Z [mm]
023-1	0.19028	−0.06133	−0.34073	0.19263	−0.06926	−0.34490	0.18705	−0.11086	−0.34656
023-2	0.19056	−0.06134	−0.34078	0.19292	−0.06925	−0.34492	0.18733	−0.11086	−0.34659
023-3	0.19077	−0.06114	−0.34089	0.19311	−0.06905	−0.34494	0.18753	−0.11067	−0.34663
023-4	0.19078	−0.06086	−0.34100	0.19311	−0.06877	−0.34495	0.18753	−0.11039	−0.34665
023-5	0.19059	−0.06065	−0.34103	0.19290	−0.06857	−0.34494	0.18734	−0.11019	−0.34664
023-6	0.19030	−0.06064	−0.34098	0.19262	−0.06858	−0.34492	0.18706	−0.11019	−0.34661
023-7	0.19009	−0.06083	−0.34086	0.19242	−0.06878	−0.34490	0.18686	−0.11038	−0.34657
023-8	0.19008	−0.06112	−0.34076	0.19243	−0.06906	−0.34489	0.18686	−0.11066	−0.34655
026-1	0.19168	−0.06069	−0.34280	0.19463	−0.06844	−0.34713	0.18922	−0.11004	−0.34864
026-2	0.19149	−0.06045	−0.34282	0.19443	−0.06822	−0.34713	0.18904	−0.10981	−0.34863
026-3	0.19152	−0.06016	−0.34291	0.19445	−0.06792	−0.34714	0.18906	−0.10952	−0.34865
026-4	0.19176	−0.05997	−0.34300	0.19467	−0.06773	−0.34715	0.18929	−0.10933	−0.34867
026-5	0.19205	−0.06000	−0.34304	0.19496	−0.06774	−0.34716	0.18959	−0.10936	−0.34869
026-6	0.19224	−0.06023	−0.34302	0.19516	−0.06797	−0.34716	0.18977	−0.10959	−0.34870
026-7	0.19221	−0.06053	−0.34293	0.19514	−0.06826	−0.34716	0.18974	−0.10988	−0.34868
026-8	0.19198	−0.06072	−0.34284	0.19492	−0.06846	−0.34715	0.18952	−0.11007	−0.34866
11B-1	0.17442	−0.05467	−0.33993	0.17718	−0.06385	−0.34491	0.17205	−0.10487	−0.34594
11B-2	0.17477	−0.05345	−0.33846	0.17747	−0.06320	−0.34318	0.17239	−0.10417	−0.34427
11B-3	0.17562	−0.05153	−0.33828	0.17823	−0.06149	−0.34241	0.17322	−0.10248	−0.34358
11B-4	0.17644	−0.05008	−0.33949	0.17899	−0.05978	−0.34306	0.17402	−0.10083	−0.34427
11B-5	0.17678	−0.04990	−0.34139	0.17933	−0.05902	−0.34475	0.17436	−0.10015	−0.34595
11B-6	0.17643	−0.05112	−0.34286	0.17904	−0.05967	−0.34648	0.17401	−0.10085	−0.34761
11B-7	0.17558	−0.05304	−0.34304	0.17829	−0.06138	−0.34725	0.17318	−0.10254	−0.34830
11B-8	0.17476	−0.05449	−0.34183	0.17753	−0.06309	−0.34660	0.17238	−0.10419	−0.34761

References

- Sarıyakupoğlu, T. Usage of Additive Manufacturing and Topology Optimization Process for Weight Reduction Studies in the Aviation History. *Adv. Sci. Technol. Eng. Syst. J.* **2021**, *6*, 815–820. [\[CrossRef\]](#)
- Scaccabarozzi, D.; Saggin, B.; Alberti, E. Design and Testing of a Roto-Translational Shutter Mechanism for Planetary Operation. *Acta Astronaut.* **2014**, *93*, 207–216. [\[CrossRef\]](#)
- Shatalina, I.; Saggin, B.; Scaccabarozzi, D.; Panzeri, R. MicroMIMA FTS: Design of Spectrometer for Mars Atmosphere Investigation. In Proceedings of the XVIII SPIE Remote Sensing of Clouds and the Atmosphere, Dresden, Germany, 17 October 2013. [\[CrossRef\]](#)
- Satya Hanush, S.; Manjaiah, M. Topology Optimization of Aerospace Part to Enhance the Performance by Additive Manufacturing Process. *Mater. Today Proc.* **2022**, *62*, 7373–7378. [\[CrossRef\]](#)
- Williams, J.C.; Starke, A.E. Progress in Structural Materials for Aerospace Systems. *Acta Mater.* **2003**, *51*, 5775–5779. [\[CrossRef\]](#)
- Zhu, J.-H.; Zhang, W.-H.; Xia, L. Topology Optimization in Aircraft and Aerospace Structures Design. *Arch. Comput. Methods Eng.* **2016**, *23*, 595–622. [\[CrossRef\]](#)
- Ooms, T.; Vantghem, G.; Thienpont, T.; Van Coile, R.; De Corte, W. Compliance-based Topology Optimization of Structural Components Subjected to Thermo-mechanical Loading. *Struct. Multidiscip. Optim.* **2023**, *66*, 126. [\[CrossRef\]](#)
- Chen, Y.; Wang, Q.; Wang, C.; Gong, P.; Shi, Y.; Yu, Y.; Liu, Z. Topology Optimization Design and Experimental Research of a 3D-Printed Metal Aerospace Bracket Considering Fatigue Performance. *Appl. Sci.* **2021**, *11*, 6671. [\[CrossRef\]](#)
- Li, H.; Liu, R.; He, S.; Xin, R.; Wang, H.; Yu, Z.; Xu, Z. Bionic Design of the Vertical Bracket of Wide Angle Auroral Imager by Additive Manufacturing. *Appl. Sci.* **2022**, *12*, 5274. [\[CrossRef\]](#)
- Berrocal, L.; Fernández, R.; González, S.; Perriñán Santos Tudela, A.; Vilanova, J.; Rubio, L.; Márquez, J.M.M.; Guerrero, J.; Lasagni, F. Topology Optimization and Additive Manufacturing for Aerospace Components. *Prog. Addit. Manuf.* **2019**, *4*, 83–95. [\[CrossRef\]](#)
- Seabra, M.; Azevedo, J.; Araújo, A.; Reis, L.; Pinto, E.; Alves, N.; Santos, R.; Mortágua, J.P. Selective Laser Melting (SLM) and Topology Optimization for Lighter Aerospace Components. *Procedia Struct. Integr.* **2016**, *1*, 289–296. [\[CrossRef\]](#)
- Shapiro, A.A.; Borgonia, J.P.; Chen, Q.N.; Dillon, R.P.; McEnerney, B.; Polit-Casillas, R.; Soloway, L. Additive Manufacturing for Aerospace Flight Applications. *J. Spacecr. Rocket. Spec. Sel. Adv. Small Satell. Technol. Appl.* **2016**, *53*, 952–959. [\[CrossRef\]](#)

13. Herrera, A.C. Optimization Driven Design and Additive Manufacturing Applied for ESA Sentinel-1 Antenna Bracket. In Proceedings of the 9th UK Altair Technology Conference, Stratford-Upon-Avon, UK, 16 June 2015. Available online: https://cdn2.hubspot.net/hubfs/47251/UKATC2015_RUAG.pdf?t=1490380914857 (accessed on 24 October 2023).
14. Harvey, B. *ExoMars*; Springer: Cham, Switzerland, 2021. [[CrossRef](#)]
15. Vago, J.; Witasse, O.; Svedheim, H.; Baglioni, P.; Haldemann, A.; Gianfiglio, G.; Blancquaert, T.; McCoy, D.; de Groot, R. ESA ExoMars Program: The Next Step in Exploring Mars. *Sol. Syst. Res.* **2015**, *49*, 518–528. [[CrossRef](#)]
16. Rodionov, D.; Zelenyi, L.; Korablev, O.; Chulkov, I.; Anufreychik, K.; Marchenkov, K.; and Vago, J. ExoMars-2020 Landing Platform Scientific Payload. In Proceedings of the EGU General Assembly 2020, Online, 4–8 May 2020. [[CrossRef](#)]
17. Scaccabarozzi, D.; Tarabini, M.; Almasio, L.; Saggin, B.; Esposito, F.; Cozzolino, F. Characterization of a Pumping System in Martian-like Environment. In Proceedings of the IEEE International Workshop on Metrology for Aerospace (MetroAeroSpace), Benevento, Italy, 12 May 2014. [[CrossRef](#)]
18. Scaccabarozzi, D.; Saggin, B.; Pagliara, C.; Magni, M.; Tarabini, M.; Esposito, F.; Molfese, C.; Cozzolino, F.; Cortecchia, F.; Dolnikov, G.; et al. MicroMED, Design of a Particle Analyzer for Mars. *Measurements* **2018**, *122*, 466–472. [[CrossRef](#)]
19. Scaccabarozzi, D.; Saggin, B.; Somaschini, R.; Magni, M.; Valnegri, P.; Esposito, F.; Molfese, C.; Cozzolino, F.; Mongelluzzo, F. MicroMED Optical Particle Counter: From Design to Flight Model. *Sensors* **2020**, *20*, 611. [[CrossRef](#)]
20. Mongelluzzo, G.; Esposito, F.; Cozzolino, F.; Molfese, F.; Silvestro, S.; Ionut Popa, C.; Dall’Ora, M.; Lubieniecki, M.; Cortecchia, F.; Saggin, B.; et al. Optimization of the Fluid Dynamic Design of the Dust Suite-MicroMED Sensor for the ExoMars 2020 Mission. In Proceedings of the IEEE International Workshop on Metrology for Aerospace (MetroAeroSpace), Rome, Italy, 20 June 2018. [[CrossRef](#)]
21. Mongelluzzo, G.; Esposito, F.; Cozzolino, F.; Molfese, C.; Silvestro, S.; Franzese, G.; Ionut Popa, C.; Lubieniecki, M.; Cortecchia, F.; Saggin, B.; et al. CFD Analysis and Optimization of the MicroMED for the ExoMars 2020 Mission. *Measurements* **2019**, *147*, 106824. [[CrossRef](#)]
22. Mongelluzzo, G.; Esposito, F.; Cozzolino, F.; Franzese, G.; Ruggeri, A.C.; Porto, C.; Molfese, C.; Scaccabarozzi, D.; Saggin, B. Design and CFD Analysis of the Fluid Dynamic Sampling System of the MicroMED Optical Particle Counter. *Sensors* **2019**, *19*, 5037. [[CrossRef](#)] [[PubMed](#)]
23. Corti, M.G.; Scaccabarozzi, D.; Saggin, B.; Valnegri, P.; Esposito, F.; Cozzolino, F.; Mongelluzzo, G. Topology Optimization of the Optical Bench for the MicroMED Dust Analyzer. In Proceedings of the IEEE International Workshop on Metrology for Aerospace (MetroAeroSpace), Naples, Italy, 23 June 2021. [[CrossRef](#)]
24. Bendsøe, M.P.; Sigmund, O. *Topology Optimization: Theory, Methods, and Applications*, 2nd ed.; Springer: Berlin, Germany, 2011. [[CrossRef](#)]
25. Gandhi, Y.; Minak, G. A Review on Topology Optimization Strategies for Additively Manufactured Continuous Fiber-Reinforced Composite Structures. *Appl. Sci.* **2022**, *12*, 11211. [[CrossRef](#)]
26. Kandemir, V.; Dogan, O.; Yaman, U. Topology Optimization of 2.5D Parts Using the SIMP Method with a Variable Thickness Approach. *Procedia Manuf.* **2018**, *17*, 29–36. [[CrossRef](#)]
27. Fetisov, K.V.; Maksimov, P.V. Topology Optimization and Laser Additive Manufacturing in Design Process of Efficiency Lightweight Aerospace Parts. *J. Phys. Conf. Ser.* **2018**, *1015*, 052006. [[CrossRef](#)]
28. European Cooperation for Space Standardization (ECSS). Space Engineering: Mechanisms—ECSS-E-ST-33-01C. ESA-ESTEC, Noordwijk. 2019. Available online: <https://ecss.nl/standard/ecss-e-st-33-01c-rev-2-1-march-2019-space-engineering-mechanisms/> (accessed on 24 October 2023).

Disclaimer/Publisher’s Note: The statements, opinions and data contained in all publications are solely those of the individual author(s) and contributor(s) and not of MDPI and/or the editor(s). MDPI and/or the editor(s) disclaim responsibility for any injury to people or property resulting from any ideas, methods, instructions or products referred to in the content.